

DISCRETE X-RAY SIGNATURES OF A PHOTOIONIZED PLASMA ABOVE THE ACCRETION DISK OF THE NEUTRON STAR EXO 0748-676

M. A. JIMENEZ-GARATE

N. S. SCHULZ

H. L. MARSHALL

MIT Center for Space Research, 70 Vassar St, NE80 6th floor, Cambridge, MA 02139
 mario@alum.mit.edu, nss@space.mit.edu, hermanm@space.mit.edu

Accepted to the Astrophysical Journal

ABSTRACT

During the disk-mediated accretion phase, the high-resolution X-ray spectrum of the low-mass X-ray binary system EXO 0748-676 reveals a photoionized plasma which is orbiting the neutron star. Our observations with the *Chandra* High Energy Transmission Grating Spectrometer (HETGS) constrain the structure of the upper layers of the accretion disk, by means of the recombination emission lines from the H-like and He-like ions of O, Ne, and Mg, which have a mean velocity broadening $\sigma_v \sim 750 \pm 120 \text{ km s}^{-1}$. The Mg XI emission region has density $n_e \gtrsim 10^{12} \text{ cm}^{-3}$ and is located within $7 \times 10^9 < r < 6 \times 10^{10} \text{ cm}$ of the neutron star, while the temperature of the Ne X region is $kT \lesssim 20 \text{ eV}$. These lines favor a vertically stratified distribution of ions in the disk. The spectra show that the line region is spatially extended and unabsorbed, while the continuum region is compact and heavily absorbed. The absorber has variable column density and is composed of both neutral and ionized gas, which can explain the stochastic and periodic X-ray intensity dips, the X-ray continuum evolution, and the O VII and Mg XI K-shell absorption edges. The absorber is located 8° – 15° above the disk midplane, inclusive of two bulges near the disk edge. This outer disk gas may participate in the outflow of ionized plasma which was previously identified in *XMM-Newton* grating spectra obtained during type I bursts. The thickened photoionized region above the disk can be produced by heating from the neutron star X-rays and by the impact of the accretion stream.

Subject headings: X-rays: binaries — line: identification — accretion, accretion disks — binaries: eclipsing

1. INTRODUCTION

EXO 0748-676 provides a unique view of a photoionized plasma in the region near an accretion disk. EXO 0748-676 is a Low-Mass X-ray Binary (LMXB) which exhibits eclipses, type I X-ray bursts, and intensity dips (Parmar et al. 1985; Parmar, White, Giommi, & Gottwald 1986). The X-ray eclipses have a period $P_{\text{orb}} = 3.82 \text{ hr}$ and last for 8.3 min. Assuming Roche lobe overflow and a primary accretor with $M_{\text{NS}} \sim 1.4 M_\odot$, Parmar et al. obtained a companion mass of $0.08 < M_C < 0.45 M_\odot$. They found that the largest M_C corresponds to a main-sequence companion, with a system inclination of $75^\circ < i < 83^\circ$. As we will see below, this inclination is favorable for X-ray spectroscopic studies of the accretion flow. The type I bursts are due to a thermonuclear flash on the surface of an accreting neutron star, which requires a magnetic field $B \lesssim 10^{10} \text{ G}$ (Lewin, van Paradijs, & Taam 1995, and references therein). The X-ray burst luminosity is near the Eddington limit, for a distance to EXO 0748-676 of $D \sim 10 \text{ kpc}$, so we will assume this value of D . The low B implies that the accretion disk can extend all the way in, down to the neutron star surface. The persistent X-ray luminosity is $L \sim 10^{37} \text{ ergs s}^{-1}$, and most of this power is released in the innermost radii of the accretion disk and in the boundary layer of the neutron star.

Intensity dips are often present in LMXB observed at high-inclination (Frank, King, & Lasota 1987). Frank et al. attributed the X-ray intensity dips to absorption

from photoionized clouds in a two-phase medium above the outer accretion disk. In EXO 0748-676, dips are associated with X-ray spectral evolution. The dips are observed to precede eclipses at orbital phase $\phi \sim 0.9$, or to occur during mid-orbit at $\phi \sim 0.6$. The depth and duty cycle of the dips varies with each orbit. During the dips, the spectrum hardens, as would be expected if they are caused by increased photoelectric absorption (Parmar, White, Giommi, & Gottwald 1986). A soft X-ray excess was observed at $8 < \lambda < 30 \text{ \AA}$ with *ASCA* and *ROSAT* (Thomas et al. 1997; Schulz 1999). This excess was presumed to be associated with the existence of two emission components, or with the “partial covering” of the X-ray source by a rapidly variable low-metallicity absorber (Parmar, White, Giommi, & Gottwald 1986; Church, Balucinska-Church, Dotani, & Asai 1998).

High-resolution 10 – 23 \AA spectra of EXO 0748-676 showed broad X-ray line emission and drastic spectral variability. Cottam et al. (2001, hereafter C01) found recombination lines from N VII, O VII, O VIII, Ne IX, and Ne X, using the *XMM-Newton* Reflection Grating Spectrometer (RGS). The K edges of O VII and O VIII were visible during the rapid variation periods, but they faded as the soft continuum dimmed. The velocity broadening of the recombination lines was $\sim 10^3 \text{ km s}^{-1}$, and it was found to be correlated with the ionization parameter. C01 concluded that both emission and absorption features originate from an extended, oblate structure above the accre-

tion disk.

A 335 ks-long exposure of EXO 0748-676 obtained with the *XMM-Newton* RGS also revealed that the cumulative spectrum of 28 type I bursts contains absorption lines which may be identified with Fe XXV and Fe XXVI at a redshift of $z = 0.35$ (Cottam, Paerels & Mendez 2002). These spectral features could represent the first measurement of a gravitational redshift from the surface of a neutron star, constraining M_{NS}/R_{NS} and the nuclear equation of state at high density. The spectra of the 5 type I bursts detected with the *Chandra* High Energy Transmission Spectrometer (HETGS) will be presented elsewhere (Marshall et al., in preparation).

In this work, we use the *Chandra* HETGS to perform a spectroscopic analysis of EXO 0748-676 during epochs exclusive of bursts in order to study the circumsource medium of the neutron star, and to constrain the elemental abundances of the accreting matter. The broadband high-resolution spectra of the HETGS, from $1.5 < \lambda < 25 \text{ \AA}$, allows us to identify the nature of the absorber which produces the intensity dips. We measure the density, location, and kinematics of the recombination line region, which constrain models of accretion disk structure.

2. *Chandra* HETGS DATA REDUCTION

The observation was performed on 2001 April 14, with a 47.7 ks exposure (starting at Modified Julian Day 52013.052). Our data was obtained with the HETGS (Canizares et al. 2000), which provides two independent spectra: the high-energy grating (HEG) spectrum has a resolution of $\Delta\lambda = 0.012 \text{ \AA}$ (FWHM), and the medium-energy grating (MEG) spectrum has a $\Delta\lambda = 0.023 \text{ \AA}$. We restrict our attention to the $1.5 < \lambda < 14 \text{ \AA}$ portion of the HEG spectrum and the $2.0 < \lambda < 25 \text{ \AA}$ portion of the MEG spectrum. The photons were detected with the Advanced CCD Imaging Spectrometer (ACIS-S) detector. The data were processed to level 2 with the CIAO tools version 2.2.1,¹ using the default spatial and pulse-height extraction regions for the HEG and MEG spectra. We used the *lightcurve* tool to histogram the count rate as a function of event time. We used the *dmscopy* tool to select time cuts from the event list. We produced event lists for two different states which were selected by count rate. We generated an effective area for each event list selection, as well as the exposure maps needed to obtain fluxed spectra using *mkgrarf*. The rebinning and fitting of spectra were performed using the ISIS program (Houck & Denicola 2000). Spectra from the +1 and -1 grating orders were combined to obtain the total HEG and MEG spectra. These spectra are fit simultaneously with phenomenological models. The HEG and MEG spectra are summed for display purposes only, since their line response functions differ considerably.

We performed continuum fits on the HETGS spectra and searched for discrete features. Our criteria for the identification of a discrete spectral feature are that 1) the number of counts in the line represents a $> 3\sigma$ deviation from the continuum level, 2) the equivalent width (EW) of the feature is consistent in both HEG and MEG spectra when both gratings have sufficient counts, or else that the feature is observed in the +1 and -1 orders of the grating

with the largest effective area, 3) the feature does not fall within a chip gap, and 4) the identified feature is spectroscopically tenable. We determined limits on some of the expected features. The unidentified residuals may, in some cases, be due to instrumental effects. Effective area systematic errors are not included in our plots. Systematic errors are occasionally visible in the 5.4 to 6.2 \AA region due to uncertainties at the Ir M-shell edges.

3. LIGHT CURVES

The X-ray light curve of EXO 0748-676 exhibits eclipses, intensity dips, and type I bursts. Previous observations of EXO 0748-676 with low spectral resolution instruments (Parmar, White, Giommi, & Gottwald 1986; Thomas et al. 1997) yielded light curves which resemble the HETGS broadband light curve in Figure 1. We split the HETGS light curve into three wavebands. The HETGS wavebands have sharp, resolution-limited boundaries ($\Delta\lambda = 0.020 \text{ \AA}$).

The appearance of the light curve varies from one waveband to another (as shown in Figure 2). Both the behavior of the light curves and the spectroscopic data presented below indicate that this variation is mainly due to intensity dips. In the 1.5 to 3 \AA band, the X-ray flux is nearly constant outside the eclipse and burst epochs, and only traces of dips are discernible. Most of the variability in the hard band of the persistent light curve is statistical. Significant changes in the accretion rate are not discernible in the light curve. We observe four eclipses, each lasting $500 \pm 10 \text{ s}$. We find five type I X-ray bursts which are each $t \lesssim 10^2 \text{ s}$ in duration. At least some of the variation of burst brightness appears to be due to a variable absorbing column of gas in the line-of-sight, since the dimmest burst (the fifth in time order) occurs during a pre-eclipse dip phase. The second-dimmest burst (also the second in time) occurs just before a pre-eclipse dip. In the 3 to 6 \AA band, there are two types of dips, stochastic and periodic. The periodic dips occur at mid-orbit ($\phi \sim 0.6$) and before eclipse ingress ($\phi \sim 0.9$). The light curve evolves with each successive binary orbit. The evolution of the dips from one binary orbit to the next indicates that the accretion flow geometry is changing at the outer edge of the accretion disk. Above 6 \AA , the light curve appears to have “soft flare” events (Bonnet-Bidaud et al. 2001, C01), one of which is in our data near the 8 ks mark. Alternatively, these “soft flares” can be explained by the variability of the absorber column, which is found in the high-resolution spectra (§4). Above 6 \AA , the eclipse ingresses appear to fade away because of deep pre-eclipse dips. In contrast, the eclipse egresses do appear in the $\lambda > 6 \text{ \AA}$ light curve because dips are shallow at those times.

The intensity dip timescale is shorter than the size of the bins in the HETGS light curve ($< 50 \text{ s}$). There are rapid intensity fluctuations which drive the count rate from maximum to minimum, or an order of magnitude change in the soft ($\lambda > 6 \text{ \AA}$) band, as shown in Figure 2. These fluctuations are common in the data and are statistically significant.

We obtain spectra for selected time intervals, with cuts based on the light curve, to isolate events during the deep dip state, the persistent (or shallow dip) state, the eclipses,

¹ CIAO is the *Chandra* Interactive Analysis of Observations, a software system developed by the *Chandra* X-Ray Center.

and the burst events. To make the cuts, we use the light curve for $\lambda > 6 \text{ \AA}$ in Figure 2. First, we exclude the times during bursts and eclipses. Then, we set a fiducial cut at $0.3 \text{ counts s}^{-1}$, below which we obtain the *dip state* with an exposure of 29.5 ks, and above which we obtain the *persistent state*, with 15.7 ks.

4. HIGH-RESOLUTION X-RAY SPECTROSCOPY OF DIP AND PERSISTENT STATES

The HETGS X-ray spectra reveal emission and absorption features which evolve with the soft X-ray intensity. The EW of the lines and the edge depths are larger during the dip state than during the persistent state. However, the line fluxes remain constant. The intensity dip spectra are best fit by an absorber composed of both neutral and ionized gas. Figure 3 shows the combined HEG and MEG spectra. The spectra require three emission components: (1) a bright, hard, power-law continuum; (2) a dim, soft continuum; and (3) a recombination emission component with resolved velocity broadening. Components 2 and 3 have a smaller absorbing column than component 1.

The observed discrete emission is produced by electron-ion recombination in a photoionized plasma. The lines detected with the largest statistical significance, as well as upper limits for selected lines, are listed in Table 1. The recombination features consist of lines from H-like and He-like ions plus radiative recombination continua (RRC). The most prominent lines in the HETGS spectra are the Mg XI and the Ne IX intercombination (*i*) lines, and O VIII Ly α . Mg XII Ly α , Ne X Ly α , Ne X RRC, Ne IX RRC, and O VII *i*+*r* are weaker but still detected with a significance $> 3\sigma$. Possible detections include Si XIV Ly α , Ne X Ly β , N VII RRC, and O VIII RRC. Collectively, these features reveal the presence of a photoionized plasma, which also produces absorption edges of O VII and Mg XI in the spectra. The fluorescence lines (Si K α , S K α , and Fe K α) are not detected at the 3σ level. The recombination lines have larger EWs during dips, because the X-ray continuum is weaker during the dip states than during the persistent states.

In the following, we constrain the density, temperature, and dynamics of the photoionized plasma. We measure the elemental abundance ratios in the emitting plasma. We also test continuum models for the dip and persistent state spectra, and we identify the ionization level of the absorber.

4.1. Diagnostics with Helium-like ion lines

We detect emission from three He-like ions: O VII, Ne IX, and Mg XI. The He α lines are shown in Figures 8, 9, and 10. The He α line ratios can be used to determine the dominant heating mechanism in the plasma (Liedahl 1999). The He α line complex can also be used to constrain the electron density (n_e) and/or the ambient UV flux (Gabriel & Jordan 1969; Blumenthal, Drake, & Tucker 1972). Three lines in the He α complex are resolvable with the HETGS: the resonance line (*r* denotes $2^1P_1 \rightarrow 1^1S_0$), the intercombination line (*i* denotes the two blended transitions $2^3P_{1,2} \rightarrow 1^1S_0$), and the forbidden line (*f* denotes $2^3S_1 \rightarrow 1^1S_0$). The notation $n^{2S+1}L_J$ identifies each two-electron atomic state, with quantum numbers n , L , S , and

J . Weak satellite lines are also present in the He α complex.

In EXO 0748-676, the *i* line dominates all the He α complexes. The *r* and *f* lines are not detected, perhaps with the exception of the *r* line of O VII, for which a few photons are detected. We now discuss the consequences of the observed He α line ratios.

The plasma must be heated by photoionization. In a photoionized plasma, recombination is usually followed by RRC emission, and the subsequent bound electron cascades produce the line emission. This contrasts with collisionally ionized gases, for which line emission is predominantly produced after resonant excitation by electron impact. This difference is measurable by the line ratio $G = (f + i)/r$, which is $G \sim 4$ for photoionized gas and $G \lesssim 1$ for collisionally ionized gas (Liedahl 1999; Porquet & Dubau 2000). The G ratios of O VII and Ne IX measured with *XMM-Newton* RGS were interpreted by C01 as a signature of a recombining plasma. The *Chandra* HETGS data in Table 2 show that the G ratios of O VII and Ne IX are consistent with the C01 measurements, and similarly, that $G \gtrsim 3$ for Mg XI. These G ratios indicate that photoionization is the dominant heating mechanism for a wide range of ionization parameters.

The plasma density is very high, or the UV field is very intense near the He α emission region, or both. This is based on the upper limits we set on the $R = f/i$ line ratio from helium-like ions (Table 2). The R ratio of the plasma depends on the effects of electron-impact excitation at high density and/or photoexcitation by an intense UV field (Gabriel & Jordan 1969; Blumenthal, Drake, & Tucker 1972; Mewe & Schrijver 1978). In the limit of a weak UV field ($F_\lambda \ll F_\lambda^{\text{crit}}$), the density n_e is constrained to be above a critical value $n_e > n_e^{\text{crit}}$. Conversely, in the low density limit ($n_e \ll n_e^{\text{crit}}$), the net UV flux F_λ is constrained to be above a critical value $F_\lambda > F_\lambda^{\text{crit}}$ at $\lambda = 1637 \text{ \AA}$, 1270 \AA , and 1033 \AA , which correspond to the $2^3S_1 \rightarrow 2^3P_{0,1,2}$ (or $f \rightarrow i$) transitions of O VII, Ne IX, and Mg XI, respectively. Note F_λ is the UV flux local to the He α emission region in units of $\text{erg cm}^{-2} \text{ s}^{-1} \text{ \AA}^{-1}$. We conservatively estimate F_λ^{crit} by equating $w_f = w_{f \rightarrow i}$, where w_f is the $2^3S_1 \rightarrow 1^1S_0$ decay rate from Drake (1971), and $w_{f \rightarrow i}$ is the $2^3S_1 \rightarrow 2^3P_{0,1,2}$ photoexcitation rate. Kahn et al. (2001) used a similar procedure to set limits on the distance from the He α emission region to the UV source. The photoexcitation rate is

$$w_{f \rightarrow i} = \frac{\pi e^2 \lambda^3 F_\lambda f_{\text{osc}}}{h m_e c^3}, \quad (1)$$

where e , m_e are the electron charge and mass, c is the speed of light, and h is Planck's constant. We calculate $w_{f \rightarrow i}$ by using the oscillator strengths f_{osc} for the $2^3S_1 \rightarrow 2^3P_{0,1,2}$ transitions in O VII and Ne IX from Cann & Thakkar (1992) and in Mg XI from Duane Liedahl (private communication, 2002). C01 attributed the $R \sim 0$ ratio in O VII and Ne IX observed in EXO 0748-676 to electron-impact excitation, thereby setting lower limits to the density. We set both density and UV flux limits, as shown in Table 2. Photoexcitation may be important for N VI through Mg XI, and the limits we set on the UV field make up for the absence of UV spectral data. A detailed calculation of the electron populations in the $n = 2$ shell of He-like ions in photoionization equilibrium is needed to

determine accurate limits on the space of allowed values of (F_λ, n_e) .

In EXO 0748-676, the electron temperature is low compared to that of a collisionally excited gas of equivalent ionization. The G ratio of Mg XI implies an electron temperature $T < 3 \times 10^6$ K. Similarly, for Ne IX we get $T < 2 \times 10^6$ K and for O VII we get $T < 1 \times 10^6$ K. In §4.2, we improve upon the above T limits by use of the RRC.

4.2. Temperature diagnostics

We detect Ne IX RRC and Ne X RRC, at a 3σ and 4σ level respectively, which confirms that the plasma is photoionized and allows us to constrain T . Free electrons recombining with ions produce an RRC width proportional to T (Liedahl & Paerels 1996). In EXO 0748-676, the velocity broadening observed in the recombination lines implies that for the RRC, velocity and temperature broadening are of the same order. We fit the RRC profiles neglecting velocity broadening, and the resulting 3σ upper limit is $kT \lesssim 20$ eV or $T \lesssim 10^5$ K for these ions. This T is in the expected range calculated using the XSTAR (Kallman & McCray 1982) photoionized plasma equilibrium model.

4.3. Line profiles

The measured velocity broadening of the three brightest lines is consistent with a constant value of $\bar{\sigma}_v \sim 750 \pm 120$ km s $^{-1}$ (see Table 1). EXO 0748-676 and 4U 1626-67 (Schulz et al. 2001) are the only LMXB known to exhibit broadening in their soft X-ray emission lines, which are likely indicative of Kepler motion in the accretion disk. We fit the lines with Gaussian profiles using the Cash (1979) statistic, which is appropriate for Poisson errors. The statistical error on the velocity broadening is σ_v/\sqrt{N} , where N is the number of photons in the line. Due to the small number of counts, the remaining lines are not included in the computation of $\bar{\sigma}_v$ above, and instead we fix their σ_v . This is done since the Poisson fluctuations in the continuum dominate the profiles of the weakest lines.

The HETGS spectra show that the velocity broadenings (σ_v) of the lines from one ionic species to another are equal within ± 330 km s $^{-1}$. Observations of N VII, O VIII, and Ne X with the *XMM-Newton* RGS revealed a trend in σ_v with ionization state, with differences as large as 1750 ± 500 km s $^{-1}$ (C01). Our HETGS data for Ne IX, Ne X, and Mg XI, show smaller line widths than those measured with RGS and smaller differences in σ_v from one line to another (Table 1).

4.4. An absorbing medium composed of ionized and neutral gas

Our fits of the HETGS spectra show that dips can be produced by an absorbing medium composed of both neutral and ionized gas (or “warm absorber”). The medium selectively absorbs the hard X-ray continuum, but not the recombination emission, which is only absorbed by interstellar gas. We assume Solar abundances for the neutral component of the absorber.

We detect both O VII K and Mg XI K absorption edges (the edge optical depths are shown in Table 3). The O VII K edge is detected only during the persistent state, and it implies $N_{\text{OVII}} = (3.2 \pm 0.6) \times 10^{18}$ cm $^{-2}$ (Fig. 7). We also

find a Mg XI K edge (see Figs. 4 and 5). The Mg XI K edge is most prominent in the MEG grating order which is *not* affected by a chip gap. The Mg XI column density is constant or slightly increasing from the persistent to the dip state, from $N_{\text{MgXI}} = (1.6 \pm 0.6) \times 10^{18}$ cm $^{-2}$ to $N_{\text{MgXI}} = (3.6 \pm 0.7) \times 10^{18}$ cm $^{-2}$. For comparison, the N_{H} absorber on the hard continuum increases by a factor of two from the persistent to the dip state (see Tables 5 and 6).

4.5. Elemental abundance ratios derived from recombination emission

We use the method introduced by Jimenez-Garate et al. (2002) to measure the elemental abundance ratios. In this method, we use a recombination plasma model with a finely spaced distribution of ionization parameters to fit the observed emission. We calculate a grid of thermal equilibrium models versus ionization parameter ξ , using the XSTAR plasma code (Kallman & McCray 1982). We fit the differential emission measure as a function of ξ with a power-law distribution of the form

$$\text{DEM}(\xi) = \frac{\partial(\text{EM})}{\partial(\log_{10} \xi)} = K\xi^\gamma, \quad (2)$$

where $\xi = L/(n_e r^2)$, K and γ are fit parameters, and the emission measure is $\text{EM} = \int n_e^2 dV$. We use the recombination rate coefficients calculated by Liedahl (private communication) with the HULLAC code (Klapisch et al. 1977), to calculate the emission line fluxes. We fit the spectral data during the dip state, where the H-like and He-like lines of O, Ne and Mg are detected. We fit six spectral lines with four parameters: two emission measure parameters plus two abundance ratios. Thus, the fit is over-constrained. Our results are shown in Table 4. We find that the O/Ne abundance ratio is smaller than the Solar value by 3σ . The Mg/Ne ratio is within 2σ of the Solar value. We caution that the detection of more ionic species is desirable to further constrain the DEM and to make the Mg/Ne abundance measurements more robust.

Our results are consistent with the O/Ne abundance ratio estimated by C01, who defined an ionization parameter of formation to estimate the emission measure. They also estimated a Solar value for the N/Ne abundance ratio. We assign a Solar abundance to Ne.

4.6. Continuum emission

We test partial covering and two-power-law continuum model fits of the HETGS spectra. The parameters of continuum fits using a two power-law model are shown in Table 5. The parameters of the fits using a partial covering model are shown in Table 6. The fit results for both the dip and persistent states are shown. We find a very weak soft component with both models (fits without it are just marginally worse). The goodness-of-fit from the Cash statistic is the same for either model.

The partial covering model requires a change in the normalization of the hard power-law. It is not able to fit the data well with just a change in the covering fraction and N_{H} . The intensity changes by $\sim 10\%$ from the dip to the persistent state, which may be due to a change in the accretion rate. The model fits with the two power-law model for the dip state are shown in Figure 4 and for the persistent state in Figure 5. In the $1.6 < \lambda < 6.9$ Å range,

we do not find a statistically significant spectral feature, following the criteria in §2.

5. DISCUSSION

The recombination emission and the O VII and Mg XI K-shell absorption edges observed in EXO 0748-676 constrain the density and location of the photoionized plasma, which appears coincident with an outer disk thickened by X-ray radiation and by stream-disk impact. The thickened disk is not necessarily out of hydrostatic equilibrium. Aside from eclipses and type I bursts, we attribute the continuum variation to dipping due to absorption from a mix of ionized and neutral gas in the line of sight. The absorbing material is likely in the outer disk. The observed He-like ion emission lines imply that the plasma is at high density or there is a strong UV field, either of which provide evidence for the proximity of the line emission region to the accretion disk. We set a limit on the Mg/O abundance ratio implied by the absorption edges and compare the result to the ratio derived from the emission lines.

5.1. The structure and density of the absorber and the soft component

The absorber, composed of neutral and ionized gas, is located at the outer accretion disk, at a height $0.14r < h < 0.27r$ above the disk midplane, which is determined from the inclination i (see §1). Our spectral fits do not exclude the possibility that the addition of other ionized species can fully account for the absorption. The periodic dips are produced by gas just inside the Roche Lobe R_L of the neutron star. The dips at orbital phase $\phi \sim 0.9$ are produced by gas located at the point where the accretion stream impacts the disk. The dips at $\phi \sim 0.6$ may originate in a warp or bulge on the outer rim of the disk. The stochastic dips are either due to stochastic structure at the outer disk rim or are located at the inner disk. Whereas C01 reported no measured change in the K-shell absorption edges of O VII and O VIII, we find evidence for variability of the optical depth of the K-shell Mg XI edge, which is correlated with dip activity. The spectral changes imply that all the intensity variations outside eclipses and bursts are due to dips, and that these dips are produced by column density variations of the partially ionized absorber.

The soft X-ray continuum region is spatially compact, whereas the recombination emission region is extended. The emission region size can be inferred from the orbital phase variations in the light curve. C01 concluded that both continuum and line emission regions should be extended, because the 6–35 Å intensity was independent of orbital phase. An extended line region is consistent with our HETGS results, since the line fluxes are not affected by dips (the region size is measured via the line widths in §5.2). However, from the eclipse egress duration of $\lesssim 50$ s in the 6–22 Å band, we constrain the soft X-ray continuum region size to $\lesssim 3 \times 10^9$ cm. The eclipses observed with the *Rossi X-ray Timing Explorer* yielded a source size of $(1\text{--}3) \times 10^8$ cm in the 0.6–6.2 Å band (J. A. Jenkins & J. E. Grindlay, in preparation). A relative orbital speed of $v \sim 500$ km s $^{-1}$ was used in both measurements.

The ionized absorption and X-ray recombination emission can originate in the same region, as suggested by

C01. From the derived N_{MgXI} (§4.4), we find $n_e > 7 \times 10^{11} (\text{Mg}_\odot/\text{Mg}) \text{ cm}^{-3}$ for the persistent state along the line of sight, and $n_e > 2 \times 10^{12} (\text{Mg}_\odot/\text{Mg}) \text{ cm}^{-3}$ for the dip states, since the absorption region has $r < R_L$ (X_\odot and X denote the Solar and observed abundances for element X , respectively). These density limits agree with those derived for the Mg XI in emission (Fig. 11), and therefore the same region can produce the observed absorption and emission. Similarly with N_{OVII} , we set $n_e > 6 \times 10^{10} (\text{O}_\odot/\text{O}) \text{ cm}^{-3}$, which is consistent with the R ratio.

Our finding that the absorber has two components with distinct ionization parameters supports the picture proposed by Frank, King, & Lasota (1987) to explain the origin of the intensity dips in LMXBs. In this picture, the presence of episodic dips is explained by the transit of clouds embedded in a two-phase medium which is produced by photoionization.

5.2. Constraints on accretion disk properties

The spectroscopic evidence points to a recombination region which is located above the outer accretion disk. We constrain the density and location of the Mg XI emission region, based on 1) the ionization level of Mg XI calculated with photoionization equilibrium models, 2) the emission measure derived from the Mg XI He α flux, and 3) the interpretation of the Mg XI velocity broadening as circular Keplerian motion around the neutron star. We set $n_e < L_{\text{max}}/\xi_{\text{min}} r^2$, where ξ_{min} is defined such that for $\xi > \xi_{\text{min}}$, $\sim 90\%$ of the Mg XI line flux is emitted, and $L_{\text{max}} = 10^{37} \text{ erg s}^{-1}$ is the unabsorbed X-ray luminosity. The model in §4.5 yields $\log_{10} \xi_{\text{min}} \simeq 1.5$ (ξ is in units of erg cm s^{-1}). To set a lower limit on the rms value of n_e , we obtain the EM of the Mg XI-emitting plasma from the $K\xi^\gamma$ fit in Table 4. We derive upper limits for the systemic velocity of $v \lesssim 310 \text{ km s}^{-1}$ for Ne IX He α , $v \lesssim 470 \text{ km s}^{-1}$ for Mg XI He α , and $v \lesssim 790 \text{ km s}^{-1}$ for Mg XII Ly α (at 90% confidence; for the He α lines, we keep G and R fixed). Such small systemic velocities are expected if the emitting plasma is orbiting the neutron star (C01). The EWs of the double-peaked optical emission lines with FWHM $\sim 2000 \text{ km s}^{-1}$ are enhanced during X-ray eclipses, which were interpreted as emission from a disk with $r \sim 6 \times 10^{10} \text{ cm}$ (Crampton et al. 1986). For circular Kepler orbits, and in the absence of optical depth effects, $\sim 90\%$ of the line emission occurs at $r \gtrsim GM_{\text{NS}}/(2\sigma_v \sin i)^2$. This r limit is less dependent on the disk emissivity $\epsilon(r)$ than the characteristic r derived by C01. The set of r and n_e limits in Figure 11 show that the Mg XI emission region is fully consistent with a plasma in orbit inside the primary's Roche lobe. The threshold density n_e^{crit} derived from the Mg XI R ratio in §4.1 bisects the allowed n_e range.

Our measurements show that the line emission originates predominantly at the outer decade in radius. The σ_v we measured for Mg XI, Ne IX, and Ne X are in agreement with the C01 measurements for N VII. The σ_v for Ne X and O VIII reported by C01 are significantly larger than our values. Whereas C01 found a correlation between σ_v and the ionization level of the emitting ion, we find no evidence for such a correlation (see §4.3). This implies that the emissivities of different ions have similar

r dependence. In that case, for ions at a given r from the neutron star, a density gradient is needed to produce distinct ionization parameters. Instead of the radially layered ionization structure proposed by C01, we find that vertical stratification of the disk density at each radius can explain the observed line widths.

The presence of photoionized plasma at large disk radii and at a height $h \gtrsim 0.14 r$ requires a mechanism to expand the disk in the vertical direction. The disk temperature predicted by the Shakura & Sunyaev (1973) model for $r \gg R_{NS}$ is

$$T = 1.4 \times 10^4 \dot{M}_{17}^{1/4} m_{1.4}^{-1/4} r_{10}^{-3/4} \text{ K}, \quad (3)$$

and it is too low to explain the presence of the H-like and He-like ions, where \dot{M}_{17} is the accretion rate in units of 10^{17} g s^{-1} , $m_{1.4}$ is the neutron star mass in units of $1.4 M_\odot$, and r_{10} is the radius in units of 10^{10} cm . For $r \gg R_{NS}$, the Shakura & Sunyaev (1973) scale height to radius ratio is

$$h/r = 2.1 \times 10^{-2} \alpha^{-1/10} \dot{M}_{17}^{3/20} m_{1.4}^{-3/8} r_{10}^{1/8}, \quad (4)$$

which is too small to explain the absorption edges at $h/r \gtrsim 0.14$. C01 suggested through a similar argument that the disk material must be far from hydrostatic equilibrium in the vertical direction.

We propose that two mechanisms cause the disk expansion: 1) the impact of the accretion stream with the disk; and 2) the illumination from the neutron star, since the disk is heated and its scale height increases. Firstly, the ram pressure at the site of the impact of the accretion stream with the outer disk will increase the disk thickness. The increase in disk thickness depends on the ratio of the ram pressure to the outer disk pressure, as well as on the cooling timescale of the gas compared to the dynamical timescale. Theoretical calculations show that at $i = 78^\circ$, the pre-eclipse dips in EXO 0748-676 can be understood as a result of absorption from a bulge produced by disk-stream impact (Armitage & Livio 1998, and references therein). The mid-orbit dips could be due to a similar impact point at smaller radii. Secondly, as shown in Figure 11, photoionization equilibrium models show that irradiation from the observed neutron star continuum can energize the disk and produce the line emission. To illustrate this, consider that the effective temperature of the neutron star continuum is

$$T_{\text{eff}} = 1.1 \times 10^5 L_{37}^{1/4} r_{10}^{-1/2} \text{ K}, \quad (5)$$

where L_{37} is the luminosity in units of $10^{37} \text{ erg s}^{-1}$. Another effect of photoionization heating is to increase the disk photosphere scale height significantly at large radii by roughly

$$h_{\text{phot}}/h \sim (T_{\text{eff}}/T)^{1/2} \sim 3 \dot{M}_{17}^{-1/8} m_{1.4}^{1/8} L_{37}^{1/8} r_{10}^{1/8}. \quad (6)$$

Models of a centrally illuminated accretion disk atmosphere and corona, which include temperature and pressure gradients as well as radiation transfer, yield atmospheric scale heights $h/r \sim 0.11$ which are compatible with the observed ionized absorption, with model parameters $L = 10^{37.3} \text{ erg s}^{-1}$ and $r = 10^{10.8} \text{ cm}$ (Jimenez-Garate, Raymond, Liedahl, & Hailey 2001; Liedahl et al. 2001). These models show that an atmosphere heated by irradiation can produce a geometrically thickened disk in hydrostatic equilibrium.

While a detailed comparison of the data with accretion disk atmosphere models is outside the scope of this article, the models are constrained by the measured line fluxes, the line profiles, and by the DEM(ξ). For example, the behavior of the line profiles for ions at different ionization levels provides information on the disk structure. A disk in which the DEM is set by vertical stratification will yield nearly equal σ_v for all ions, while if the DEM is set by radial stratification, σ_v will increase with ξ .

5.3. UV emission from the disk can photoexcite He-like ions

We use the observed R ratio to measure the UV emission of the accretion disk, for the low density case. Having established the location of the recombination region by other means, we can use the R ratios to estimate the UV luminosity of the disk. We use the limits on F_λ at $\lambda = 1033 \text{ \AA}$, 1270 \AA , and 1637 \AA , which are local to the recombination region. The limits from photoexcitation calculations assume $n_e \ll n_e^{\text{crit}}$ and are shown in Table 2 (see also §4.1). Taking a fiducial distance between the recombination region and the disk photosphere to be $h \sim r/\tan i \sim 10^{10} \text{ cm}$, we get $L(1033\text{\AA}) > 2 \times 10^{29} h_{10}^2 \text{ erg s}^{-1} \text{\AA}^{-1}$, $L(1270\text{\AA}) > 2 \times 10^{28} h_{10}^2 \text{ erg s}^{-1} \text{\AA}^{-1}$, and $L(1637\text{\AA}) > 6 \times 10^{26} h_{10}^2 \text{ erg s}^{-1} \text{\AA}^{-1}$. The UV emission of a model disk with $L = 10^{37.3} \text{ erg s}^{-1}$ is calculated using equation (3) plus a neutron star illumination term, with the disk albedos calculated by Jimenez-Garate, Raymond, Liedahl, & Hailey (2001). The model disk luminosities (for $r \sim 10^{11} \text{ cm}$) are $L(1033\text{\AA}) \sim 7 \times 10^{31} \text{ erg s}^{-1} \text{\AA}^{-1}$, $L(1270\text{\AA}) \sim 5 \times 10^{31} \text{ erg s}^{-1} \text{\AA}^{-1}$, and $L(1637\text{\AA}) \sim 4 \times 10^{31} \text{ erg s}^{-1} \text{\AA}^{-1}$. If $r \sim 3 \times 10^{10} \text{ cm}$, $L(1637\text{\AA})$ is $\sim 20\%$ lower and $L(\lambda)$ is unchanged for $\lambda \lesssim 1400 \text{ \AA}$. We conclude that in the low density limit, the derived lower limits on the UV luminosity are fully consistent with the expected disk emission.

The effects of UV photoexcitation of $2^3S_1 \rightarrow 2^3P_{0,1,2}$ in the R ratio of low- and mid- Z He-like ions were identified in the spectra of stellar coronae and X-ray binaries. Photoexcitation was taken into account to accurately measure the density in the Solar corona with C V (Gabriel & Jordan 1969; Blumenthal, Drake, & Tucker 1972; Doyle 1980). Photoexcitation by the UV field in the vicinity of O-stars was found to overwhelm the effect of electron-impact excitation, producing $R \lesssim 0.3$ ratios of Ne IX and O VII, with evidence for similarly low R ratios of N VI and Mg XI (Kahn et al. 2001). Direct observations of X-ray and UV spectra showed that photoexcitation can account for the $R \lesssim 0.3$ ratio of N VI through Ne IX in Hercules X-1, an intermediate-mass X-ray binary (Jimenez-Garate et al. 2002). From our data and that of C01, we have shown that in EXO 0748-676, photoexcitation by the accretion disk UV emission can drive the $R \lesssim 0.2$ ratio of N VI through Mg XI.

5.4. Elemental abundance ratios derived from edges

While the Ne/O and Mg/O abundance ratios derived from our emission line model are within 3σ of Solar, the edge-derived Mg/O ratio is larger than the Solar value. The recombination line analysis implies that the EM decreases with ξ . If we assume the line-of-sight gas follows a

similar trend, then $N_{\text{MgXI}}/N_{\text{OVII}} < \text{Mg/O}$ and the abundance ratio $\text{Mg/O} > 4$ times the Solar value (3σ limit). However, the edge-derived abundances may not be as reliable as those obtained from emission lines, since the soft continuum (absorbed by O VII) and the hard continuum (absorbed by Mg XI) require distinct spectral components, so our line of sight to them may differ. There is a marginal detection of a larger-than-expected neutral Mg K edge at 9.48 Å in the spectrum of Figure 7. The abundance ratio obtained from the emission lines is $\text{Mg/O} = 10 \pm 5$ or $\text{Mg/O} = 16 \pm 9$ times Solar, depending on the model chosen (Table 4).

6. CONCLUSIONS

The *Chandra* HETGS spectra reveal discrete absorption and emission features which are the signatures of a photoionized plasma in orbit around the neutron star in EXO 0748-676. We discern a compact source of continuum X-rays with hard and soft components, as well as an extended recombination emission region originating in the outer decade in radius above the accretion disk. The recombination emission is more prominent above 8 Å and during dips, since it is less absorbed than the compact continuum emission. During three binary orbits, the color dependent X-ray light curves show that the intensity variations are due only to eclipses, type I bursts, and intensity dips, with no evidence for accretion rate changes $> 10\%$.

The high-resolution X-ray spectra show that intensity dips are caused by the increase in column density of an absorber which is composed of photoionized plasma and neutral gas. Both the Mg XI edge optical depth and N_{H} are correlated with dip activity. The signatures of the photoionized absorber are the K-shell edges of Mg XI and O VII, as well as the O VIII and O VII K-shell edges found by C01. The periodic absorber is located in two bulges of the outer accretion disk, one of which is near the accretion stream. Another component of the absorber does not correlate with orbital period. The photoionized medium also produces emission features with a large velocity broadening of $500 < \sigma_v < 1200 \text{ km s}^{-1}$, but with a small systemic velocity $v < 310 \text{ km s}^{-1}$ (at 90% confidence). The radiative recombination emission lines Mg XII Ly α , Mg XI He α , Ne X Ly α , Ne IX He α , O VIII Ly α , and O VII He α are detected, as well as the RRC of Ne X and Ne IX, which are signatures of a photoionized gas with $kT \lesssim 20 \text{ eV}$. Our line model fits imply O/Ne and Mg/Ne abundance ratios within 3σ of the Solar values. The ionized edges may, however, require a Mg/O abundance ratio $\gtrsim 4$ times Solar

(3σ).

The photoionized plasma is located at the outer decade in radius of an accretion disk which is thickened by X-ray illumination and by the impact of the accretion stream on the disk. The plasma is located at a height $h \sim 0.2r$ above and below the disk midplane, which is larger than the Shakura & Sunyaev (1973) model predictions. Spectroscopic constraints on the ionization parameter, density, kinematics, and UV radiation environment of the emitting plasma, all indicate that it is bound in Kepler orbits inside the neutron star Roche Lobe. X-ray photoionization heating from the neutron star and ram pressure from the accretion stream can sufficiently expand the disk to explain the observed geometry. Accretion disk atmosphere and corona models with vertically stratified ionization can produce disks with the required height. The ionization structure of the observed emission region can be attributed to vertical disk density gradients, with no evidence for radial temperature stratification. The measured spectra introduce stringent constraints on the accretion disk structure, and further model comparisons are warranted by the data.

We expect the spectra of the type I bursts in EXO 0748-676 to be partially absorbed by the ionized plasma in the outer accretion disk, particularly during the intensity dip phases and above $\sim 6 \text{ Å}$. The fifth burst in our HETGS observation shows evidence for such absorption (see Figs. 1 and 2). The association we found between dips and an ionized absorber implies that the ionized absorber column on the burst spectra will be largest at orbital phases $\phi \sim 0.6$ and $\phi \sim 0.9$, when a disk bulge is in the line of sight. Cottam, Paerels & Mendez (2002) reported an ionized absorber outflowing during the late burst phases, which they modeled in the spectrum to discern the gravitationally redshifted features attributed to the neutron star surface. Since the burst duration is much shorter than the outer disk dynamical timescale, this ionized absorber outflow may be produced by material in the outer accretion disk which is radiatively driven by the burst. In that case, the nature of the outflow would be closely related to the structure of the accretion disk and its time-dependent response to a type I burst.

We thank Prof. Claude Canizares, the P.I. of HETG, for providing these data as part of his Guaranteed Target Observations (GTO). We thank the members of the MIT CXC and HETG groups for their support. Funding for this work was provided under NASA contract number NAS8-01129.

REFERENCES

- Armitage, P. J. & Livio, M. 1998, *ApJ*, 493, 898
- Blumenthal, G. R., Drake, G. W. F., & Tucker, W. H. 1972, *ApJ*, 172, 205
- Bonnet-Bidaud, J. M., Haberl, F., Ferrando, P., Bennie, P. J., & Kendziorra, E. 2001, *A&A*, 365, L282
- Canizares, C. R. et al. 2000, *ApJ*, 539, L41
- Cann, N. M., & Thakkar, A. J. 1992, *Phys. Rev. A*, 46, 9, 5397
- Cash, W. 1979, *ApJ*, 228, 939
- Church, M. J., Balucinska-Church, M., Dotani, T., & Asai, K. 1998, *ApJ*, 504, 516
- Cottam, J., Kahn, S. M., Brinkman, A. C., den Herder, J. W., & Erd, C. 2001, *A&A*, 365, L277
- Cottam, J., Paerels, F., & Mendez, M. 2002, *Nature*, 420, 51
- Crampton, D., Stauffer, J., Hutchings, J. B., Cowley, A. P., & Ianna, P. 1986, *ApJ*, 306, 599
- Doyle, J. G. 1980, *A&A*, 87, 183
- Drake, G. W. F. 1971, *Phys. Rev. A*, 3, 908
- Gabriel, A. H. & Jordan, C. 1969, *MNRAS*, 145, 241
- Frank, J., King, A. R., & Lasota, J.-P. 1987, *A&A*, 178, 137
- Houck, J. C. & Denicola, L. A. 2000, in *ASP Conf. Ser.* 216, *Astronomical Data Analysis Software and Systems IX*, ed. N. Manset, C. Veillet, & D. Crabtree (San Francisco: ASP), 591
- Jimenez-Garate, M. A., Raymond, J. C., Liedahl, D. A., & Hailey, C. J. 2001, *ApJ*, 558, 448
- Jimenez-Garate, M. A., Hailey, C. J., Herder, J. W. d., Zane, S., & Ramsay, G. 2002, *ApJ*, 578, 391
- Kahn, S. M., Leutenegger, M. A., Cottam, J., Rauw, G., Vreux, J.-M., den Boggende, A. J. F., Mewe, R., & Güdel, M. 2001, *A&A*, 365, L312
- Kallman, T. R. & McCray, R. 1982, *ApJS*, 50, 263

- Klapisch, M., Schwab, J. L., Fraenkel, J. S., & Oreg, J. 1977, *Opt. Soc. Am.*, 61, 148
- Lewin, W. H. G., van Paradijs, J., & Taam, R.E. 1995, in *X-ray Binaries*, ed. W. H. G. Lewin, J. van Paradijs, & E. P. J. van den Heuvel, (Cambridge: Cambridge University Press), 175
- Liedahl, D. A. & Paerels, F. 1996, *ApJ*, 468, L33
- Liedahl, D. A. 1999, in *X-ray Spectroscopy in Astrophysics*, EADN School proceedings, ed. J. A. van Paradijs, & J. A. M. Bleeker (Amsterdam: Springer), 189
- Liedahl, D. A., Wojdowski, P., Jimenez-Garate, M. A., & Sako M. 2001, in *ASP Conf. Ser. 247, Spectroscopic Challenges of Photoionized Plasmas*, ed. G. Ferland, & D. W. Savin (San Francisco: ASP), 417
- Mewe, R. & Schrijver, J. 1978, *A&A*, 65, 99
- Parmar, A. N., White, N. E., Giommi, P., Haberl, F., Pedersen, H., & Mayor, M. 1985, *IAU Circ.*, 4039, 1
- Parmar, A. N., White, N. E., Giommi, P., & Gottwald, M. 1986, *ApJ*, 308, 199
- Porquet, D. & Dubau, J. 2000, *A&AS*, 143, 495
- Schulz, N. S. 1999, *ApJ*, 511, 304
- Schulz, N. S., Chakrabarty, D., Marshall, H. L., Canizares, C. R., Lee, J. C., & Houck, J. 2001, *ApJ*, 563, 941
- Shakura, N. I. & Sunyaev, R. A. 1973, *A&A*, 24, 337
- Thomas, B., Corbet, R., Smale, A. P., Asai, K., & Dotani, T. 1997, *ApJ*, 480, L21
- Wilms, J., Allen, A., & McCray, R. 2000, *ApJ*, 542, 914

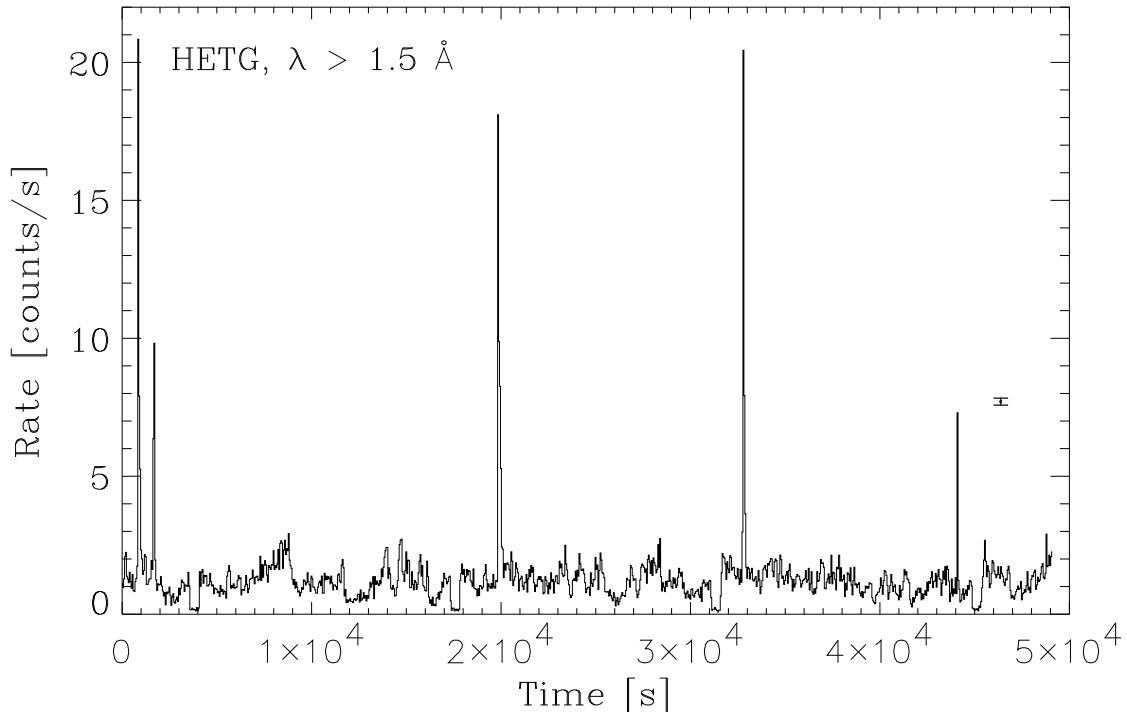


FIG. 1.— Light curve of all dispersed photons in the HETGS from the $1.5 < \lambda \lesssim 25 \text{ \AA}$ band in 50 s bins. The statistical uncertainty at a rate of 1.0 count/s is shown. The light curve shows sharp eclipse events, bright and short type I bursts, and intensity dips. The decrease in brightness of type I bursts appears to be associated with the dip events.

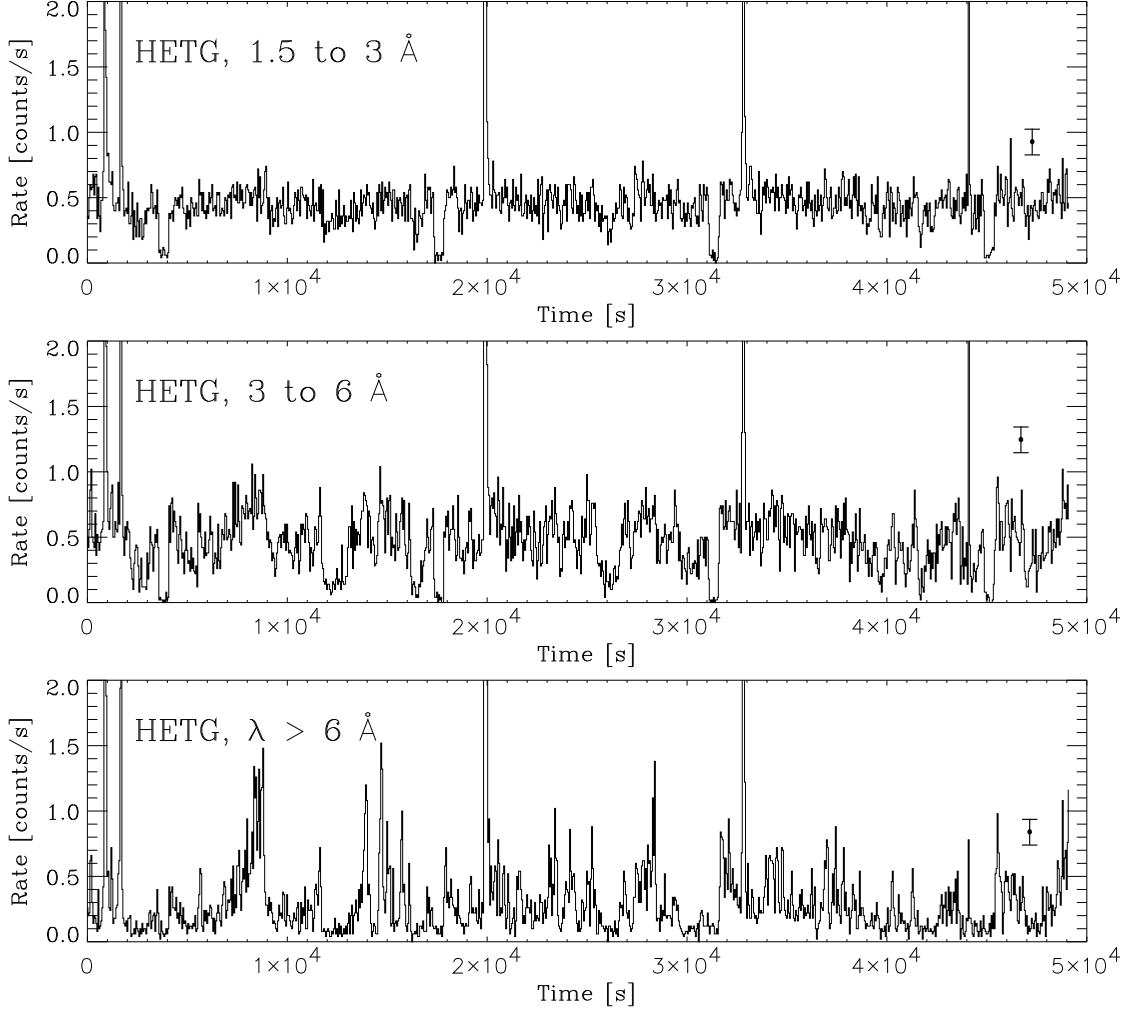


FIG. 2.— Light curves for three distinct wavelength intervals in 50 s bins. The statistical uncertainty at a rate of 0.5 counts/s is shown. The spectrum hardens during dip events, and the 1.3 Å to 3 Å light curve implies a nearly constant accretion rate. The “soft flare” at 8 ks shows the same color properties as the intervals without intensity dips.

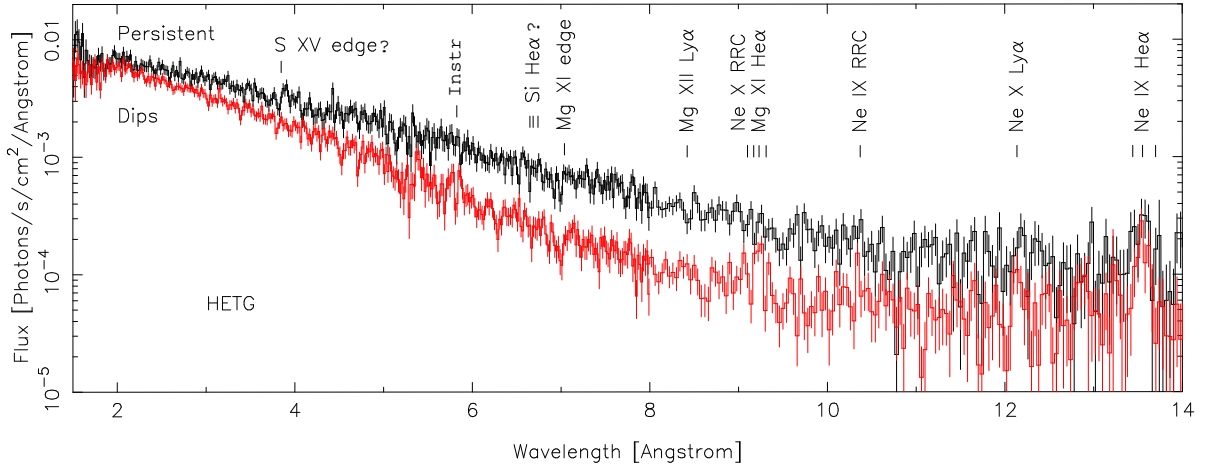


FIG. 3.— Summed MEG and HEG spectra; (top curve) 15.7 ks during the persistent state, (bottom curve) 29.5 ks during the dip state. During the dip phases, the hard continuum component is absorbed while the soft recombination lines remain unabsorbed.

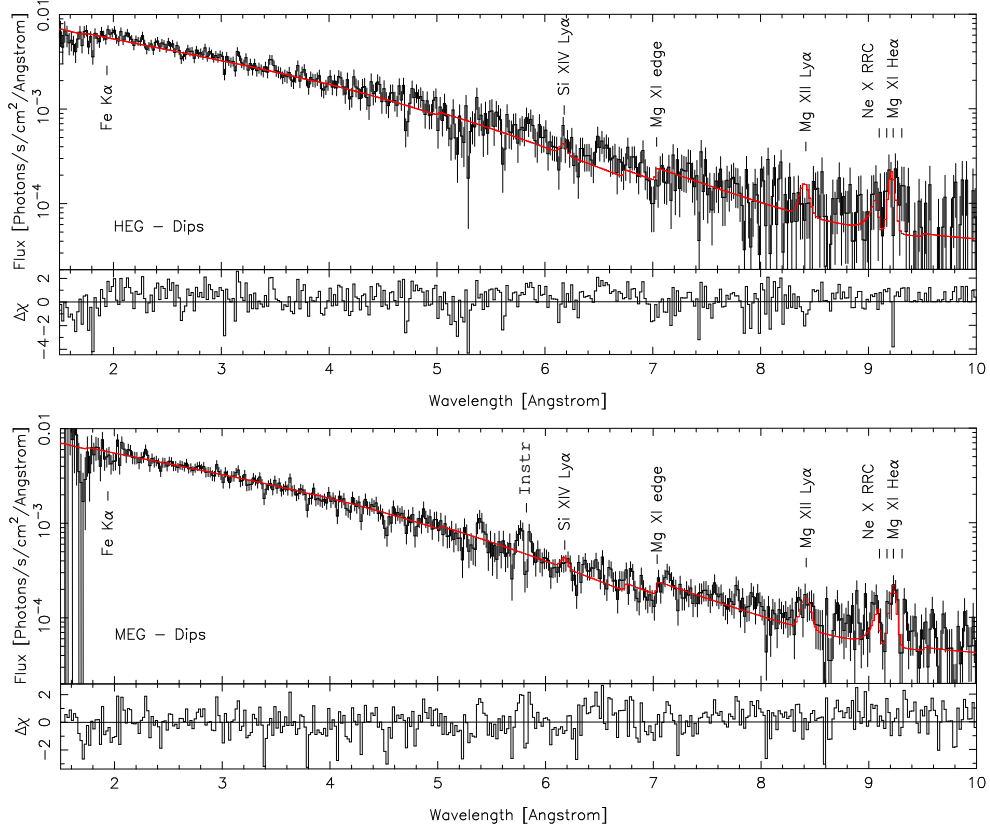


FIG. 4.— Observed spectra during the 29.5 ks dip state (black), with model fit (red), and residuals (bottom, in units of the standard deviation). Grating: (a) HEG, (b) MEG. The Mg XI *i* line and the Mg XI K edge are most prominent in the MEG spectrum. The discrete spectral features, which include RRC, are the signatures of a photoionized plasma.

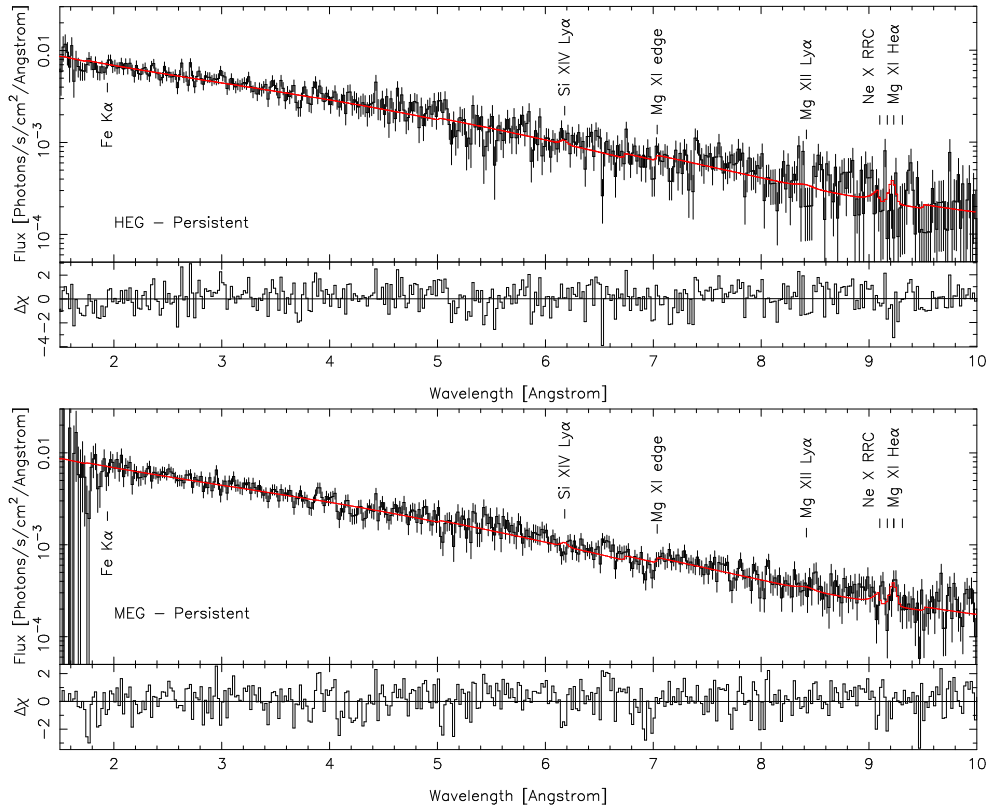


FIG. 5.— Observed spectra during the 15.7 ks persistent state (black), with model fit (red), and residuals (bottom, in units of the standard deviation). Grating: (a) HEG, (b) MEG. Here, the discrete spectral features are not as prominent as in Fig. 4.

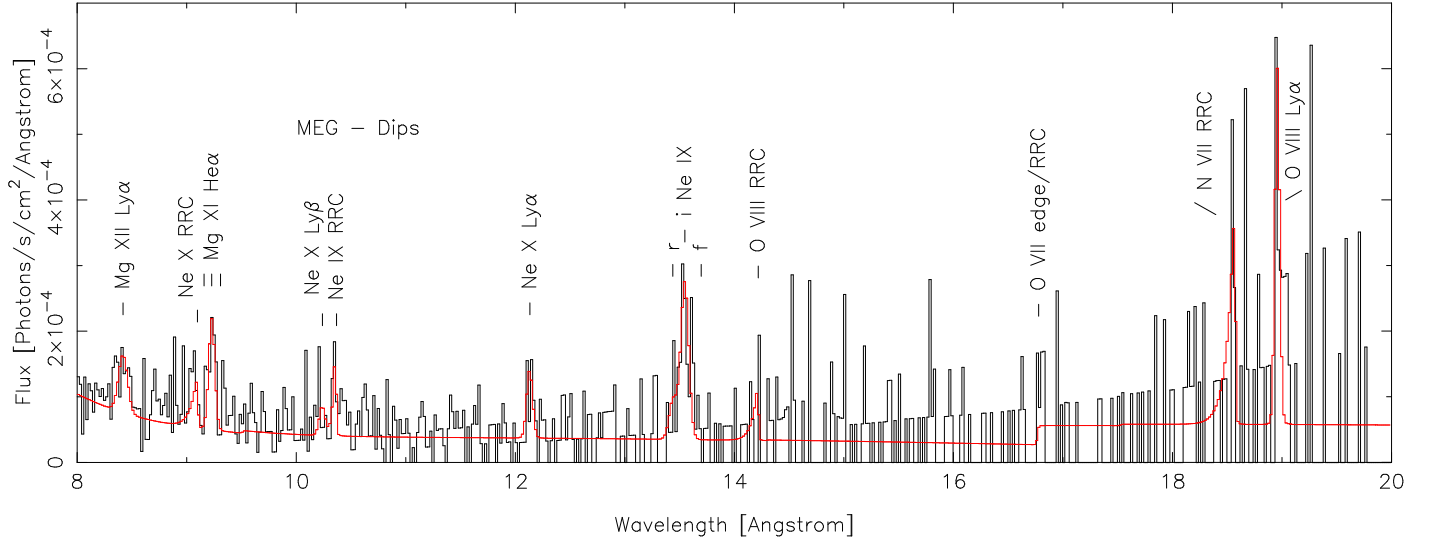


FIG. 6.— Observed MEG spectrum during the dip state (black) and model fit (red). The emission lines from H-like and He-like ions and their respective RRCs are the signatures of a photoionized plasma. The Ne IX RRC and Ne X RRC are used to constrain the temperature (§4.2).

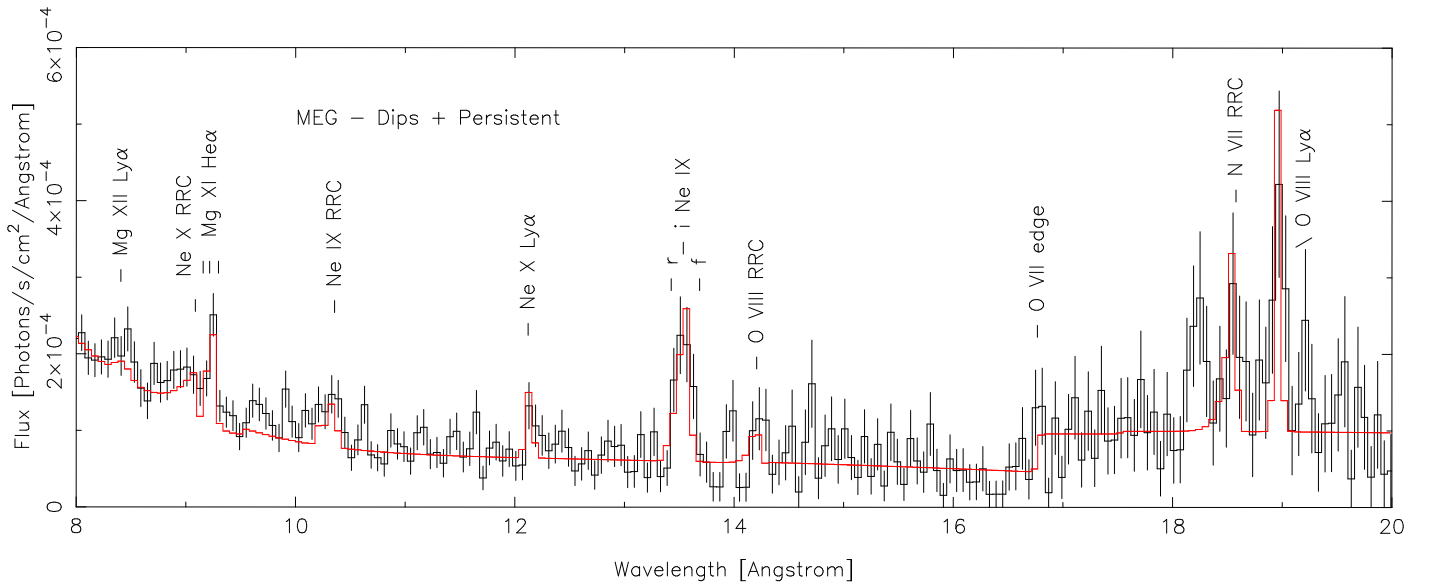


FIG. 7.— Observed MEG spectrum including both the dip and persistent states (black) and model fit (red). Bursts are excluded. The line broadening, especially discernible for Ne IX *i*, and the limits on the systemic velocity, can be explained if the plasma is orbiting the neutron star. The O VII K shell absorption edge shows that part of the material producing the intensity dips is highly ionized.

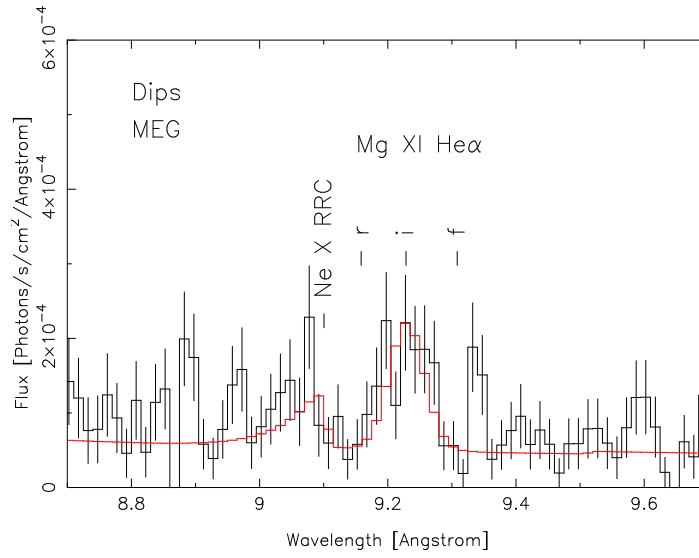


FIG. 8.— Observed MEG spectrum of the Mg XI He α line region during dip states (black) and model fit (red). The $G = (f + i)/r$ line ratio implies a photoionized plasma. The high $R = i/f$ line ratio is due to either a high electron density or a strong UV field near the accretion disk (§4.1).

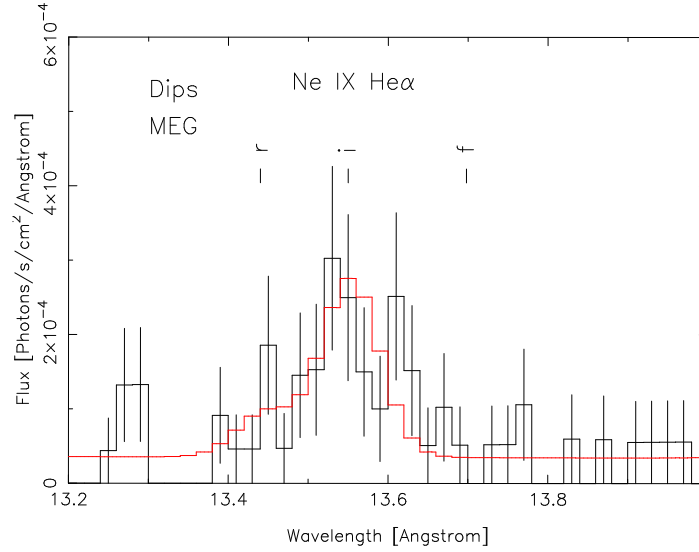


FIG. 9.— Observed MEG spectrum of the Ne IX He α line region during dip states (black) and model fit (red).

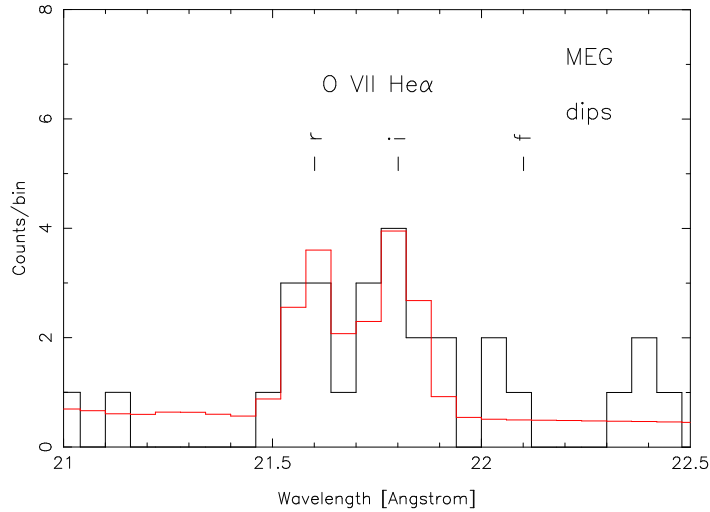


FIG. 10.— Observed MEG spectrum of the O VII He α line region during dip states (black), which shows that O VII He α is detected. The model fit is shown in red.

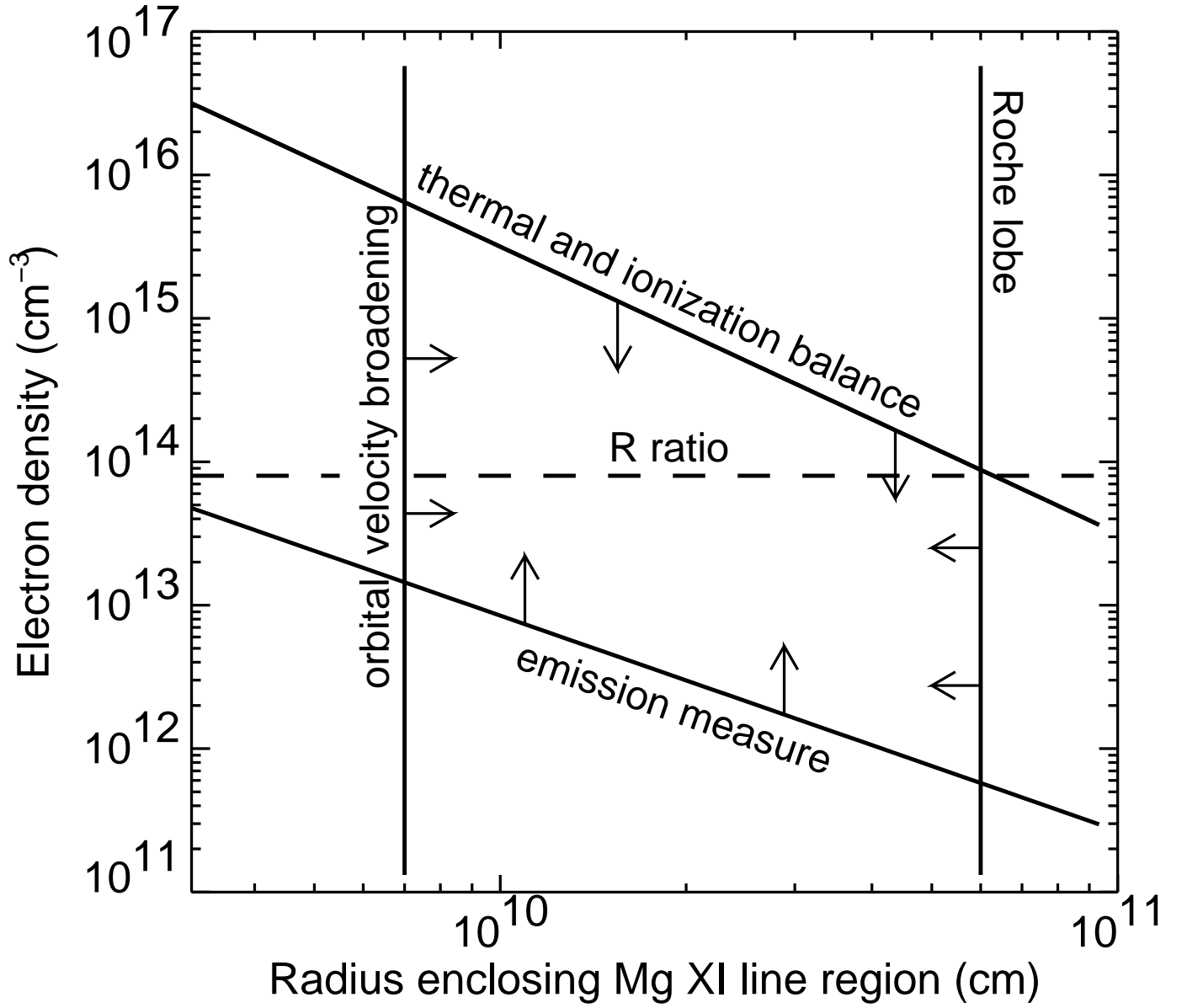


FIG. 11.— Derived limits on the region which produces the Mg XI He α recombination emission. The radius is the distance from the neutron star. The Mg XI region is located near the outer accretion disk.

TABLE 1
X-RAY EMISSION FEATURES

Feature	λ^a [Å]	σ_v [km s ⁻¹]	Flux [10 ⁻⁵ ph cm ⁻² s ⁻¹]	State
O VII <i>f</i>	22.097	700 ^a	≤ 2.4	Dip
		700 ^a	≤ 3.7	Persistent
O VII <i>i</i>	21.802	700 ^a	4.7 ± 1.9	Dip
		700 ^a	5.9 ± 3.4	Persistent
O VII <i>r</i>	21.600	700 ^a	3.4 ± 1.7	Dip
		700 ^a	≤ 1.4	Persistent
O VIII Ly α	18.970	700 ^a	3.5 ± 1.2	Dip
		700 ^a	3.7 ± 2.0	Persistent
N VII RRC	18.587	0 ^a	2.7 ± 1.2	Dip
Ne IX <i>f</i>	13.698	1200 ^a	≤ 0.4	Dip
		500 ^a	≤ 0.1	Persistent
Ne IX <i>i</i>	13.552	1200 ± 330	2.46 ± 0.61	Dip
		500 ± 270	2.21 ± 0.83	Persistent
Ne IX <i>r</i>	13.447	1200 ^a	≤ 0.48	Dip
		500 ^a	≤ 2.40	Persistent
Ne X Ly α	12.135	570 ± 250	0.69 ± 0.26	Dip
		620 ^a	≤ 1.04	Persistent
Ne IX RRC	10.370	0 ^a	0.49 ± 0.18	Dip
Ne X Ly β	10.239	900 ^a	0.35 ± 0.16	Dip
		732 ^a	≤ 0.82	Persistent
Mg XI <i>f</i>	9.314	900 ^a	≤ 0.36	Dip
		650 ^a	≤ 0.44	Persistent
Mg XI <i>i</i>	9.230	890 ± 220	1.18 ± 0.20	Dip
		650 ± 330	1.05 ± 0.41	Persistent
Mg XI <i>r</i>	9.169	900 ^a	≤ 0.43	Dip
		650 ^a	≤ 0.19	Persistent
Ne X RRC	9.102	0 ^a	0.52 ± 0.17	Dip
Mg XII Ly α	8.419	900 ^a	0.62 ± 0.22	Dip
		750 ^a	≤ 0.31	Persistent
Si XIV Ly α	6.180	900 ^a	0.51 ± 0.26	Dip
		750 ^a	≤ 0.21	Persistent

Note. — Errors and upper limits are 1σ .

^aThese values are fixed.

TABLE 2
DIAGNOSTICS WITH HE-LIKE ION LINES

Ion	Measured $R = f/i$ Line Ratio	Measured $G = (f + i)/r$ Line Ratio	Derived n_e^{crit} [cm ⁻³] ⁽¹⁾	Derived F_λ^{crit} [erg cm ⁻² s ⁻¹ Å ⁻¹] (est.)	State
Mg XI	< 0.15	> 3	8×10^{13}	2×10^9	Dip
	< 0.4	> 2	3×10^{13}	...	Persistent
Ne IX	< 0.08	> 4	1×10^{13}	...	Dip
	< 0.05	> 0.6	3×10^{13}	2×10^8	Persistent
O VII	< 0.3	2 ± 1	3×10^{11}	6×10^6	Dip
	< 0.4	> 2	2×10^{11}	...	Persistent

Note. — Errors and upper limits are 1σ . Symbols: n_e^{crit} = critical electron density, F_λ^{crit} = critical UV flux at $f \rightarrow i$ transition wavelength. C01 observed $R < 0.2$ for both O VII and Ne IX, which are consistent with our HETGS observations.

References. — (1) Porquet & Dubau 2000.

TABLE 3
X-RAY ABSORPTION FEATURES

Edge	λ [Å]	τ	State
Mg XI K	7.037 ^a	0.36 ± 0.07	Dip
		0.16 ± 0.06	Persistent
O VII K	16.78 ^a	0.76 ± 0.13	Persistent

Note. — Errors are 1σ , with the continuum parameters and N_{H} set free.

^aThese values are fixed.

TABLE 4
ELEMENTAL ABUNDANCE MEASUREMENTS AND DIFFERENTIAL EMISSION MEASURE (DEM) PARAMETERS

(O/Ne) $(\text{O}/\text{Ne})_\odot$	(Mg/Ne) $(\text{Mg}/\text{Ne})_\odot$	K (10^{58} cm^{-3})	$-\gamma$	χ^2 of Fit (o.c.)	Ionizing Spectrum
0.3 ± 0.1	4.8 ± 2.1	$4.4_{-3.0}^{+1.6}$	1.2 ± 0.4	0.28	20 keV brems.
0.4 ± 0.15	4.1 ± 2.0	$0.85_{-0.63}^{+0.30}$	0.74 ± 0.38	0.52	PL +cut

Note. — Symbols: o.c. = over-constrained fit. We show the 1σ statistical errors. The element abundance ratios (by number of atoms) are normalized to the solar values compiled by Wilms, Allen, & McCray (2000), which are $(\text{O}/\text{Ne})_\odot = 6.9$, and $(\text{Mg}/\text{Ne})_\odot = 0.32$. The K and γ parameters define the DEM. The abundance measurements depend weakly on the assumed ionizing X-ray continuum.

TABLE 5
CONTINUUM FITS FOR TWO POWER LAW MODEL

Fit parameter	Units	Value (Dips)	Value (Persistent)
PL1 Norm. (1 keV)	phot keV ⁻¹ cm ⁻² s ⁻¹	$(1.8 \pm 0.2)10^{-2}$	$(2.0 \pm 0.2)10^{-2}$
PL1 N_H	10 ²² cm ⁻²	4.2 ± 0.1	2.4 ± 0.2
PL1 Index	...	1.18 ± 0.03	1.20 ± 0.03
PL2 Norm. (1 keV)	phot keV ⁻¹ cm ⁻² s ⁻¹	$(1.4 \pm 0.1)10^{-3}$	$(2.4 \pm 0.2)10^{-3}$
PL2 N_H	10 ²² cm ⁻²	0.20 ± 0.01	0.11^a
PL2 Index	...	3.3^a	3.3 ± 0.1
Cash-stat/ DOF	...	$2155/3072 = 0.70$	$2317/3072 = 0.75$

Note. — Errors and upper limits are 1σ .

^aThese values are fixed.

TABLE 6
CONTINUUM FIT PARAMETERS FOR PARTIAL COVERING MODEL

Fit parameter	Units	Value (Dips)	Value (Persistent)
BB Norm. (1 keV)	phot keV ⁻¹ cm ⁻² s ⁻¹	$(9.3 \pm 0.9)10^{-4}$	$9.3 \times 10^{-4}^a$
BB kT	eV	2^a	2^a
BB N_H	10 ²² cm ⁻²	23 ± 2	44 ± 5
PL Cov. Frac.	...	0.976 ± 0.001	0.941 ± 0.002
PL Index	...	1.7^a	1.7^a
PL N_H	10 ²² cm ⁻²	4.60 ± 0.03	3.21 ± 0.05
PL Norm. (1 keV)	phot keV ⁻¹ cm ⁻² s ⁻¹	$(3.5 \pm 0.3)10^{-2}$	$(4.4 \pm 0.4)10^{-2}$
Cash-stat/ DOF	...	$2073/3072 = 0.68$	$2141/3072 = 0.70$

Note. — Errors and upper limits are 1σ .

^aThese values are fixed.